https://doi.org/10.5194/se-2020-8
Preprint. Discussion started: 3 March 2020

Solid Earth Discussions

Characterizing the global ocean ambient noise as recorded by the dense seismo-acoustic Kazakh network

Alexandr Smirnov[1,2], Marine De Carlo[3], Alexis Le Pichon[3], Nikolai M. Shapiro[2,4,5], Sergey Kulichkov[6]

[1]Institute of Geophysical Research, Almaty, 050020, Kazakhstan
[2]Institut de Physique du Globe de Paris, Sorbonne Paris Cité, F-75005 Paris, France
[3]CEA, DAM, DIF, F-91680 Arpajon, France
[4]Institut de Sciences de la Terre, Université Grenoble Alpes, CNRS (UMR5275), Grenoble, France.
[5]Schmidt Institute of Physics of the Earth, Russian Academy of Sciences, Moscow, Russia
[6]A.M. Obukhov Institute of Atmospheric Physics RAS, Moscow, 119017, Russia

Correspondence to: Alexandr Smirnov (smirnov@ipgp.fr)

Abstract. The dense seismo-acoustic network of the Institute of Geophysical Research (IGR), National Nuclear Center of the Republic of Kazakhstan, has been operating in Kazakhstan since the late nineties of the last century. It consists of four seismic and three infrasonic arrays. The IGR network includes stations part of several national and global monitoring systems. Infrasonic and seismic data are processed using the Progressive Multi-Channel Correlation (PMCC) detector to characterize the temporal variability of microbarom and microseism signals from 2014 to 2017. The non-linear interaction of ocean waves is simulated using the microseism source model distributed by the French Research Institute for Exploitation of the Sea (IFREMER). The wave attenuation is calculated using a semi-empirical propagation law in a range independent atmosphere. Comparing the observed and predicted seismic and infrasonic signals reveals the dominating directions of arrivals at each station of the IGR network and the associated source regions. Both multi-year and intra-seasonal parameter variations are analysed. The level of low-frequency noise is significantly higher in winter than in summer. In winter, sources of infrasound ambient noise are mainly located in the North Atlantic and in the North Pacific during Sudden Stratospheric Warming (SSW) events. Signals observed in summer, likely originating from source regions in the southern hemisphere, are discussed.

Introduction

Fundamentals to predict microseism and microbarom source regions were described by Longuett and Higgins (Longuet-Higgins, 1950). They demonstrated how counter propagating waves and their second-order nonlinear interactions can generate propagating acoustic waves in the ocean, and create seismic noise by exciting the sea floor. Hasselmann (Hasselmann, 1963, 1966) later generalized this theory to random waves, showing that the resulting acoustic frequency is twice the frequency of the ocean waves, by considering nearly opposing waves interacting.

https://doi.org/10.5194/se-2020-8
Preprint. Discussion started: 3 March 2020

Ardhuin et Herbers (Ardhuin and Herbers, 2013) developed a numerical model based on Longuett-Higgins-Hasselmann theory for the generation of Rayleigh waves, considering an equivalent pressure source at the undisturbed ocean surface. Sources of microseisms are distributed by IFREMER (IFREMER, 2018) referred to as 'p2l' – as a composite calculated from the wave-action WaveWatch III model (WW3) developed by the National Oceanic and Atmospheric Administration (NOAA). These nonlinear interactions also generate waves propagating in the atmosphere, so-called microbaroms. In this study, the source term at the ocean surface for microseisms ('p2l') and microbaroms are assumed identical (Ardhuin and Herbers, 2013; Waxler and Gilbert, 2006). The bathymetry and directivity effects are neglected in this study.

The bathymetry effect plays an important role when calculating the microseism source intensity. Longuett-Higgins (1950) showed that pressure fluctuations do not attenuate with depth but propagate to the ocean bottom as acoustic waves. Depending on the ratio between the wavelength of the acoustic waves and the ocean depth, resonance effects can occur leading to a modulation of the pressure fluctuations at the ocean bottom (Stutzmann et al., 2012).

The microbarom frequency band is at the lower edge of the frequency band of interest to monitor nuclear tests. Recent global scale microbarom observations recorded by the International Monitoring System (IMS) network of the Comprehensive nuclear Test Ban Treaty Organization (CTBTO) confirm that its detection capability is highly variable in space and time (Ceranna et al., 2018). Thus, in order to assess the microbarom source intensity accurately, it is necessary to take into account a realistic description of the middle atmosphere.

As for microseisms, microbaroms are not the impulsive signals but quasi-monochromatic sequences of permanent waves (Olson and Szuberla, 2005); therefore, it is not possible to detect their onset and identify their propagation paths. However, such signals are well detected using standard processing techniques, such as beamforming methods used from the sixties (Capon, 1972; Haubrich and McCamy, 1969; ToksoZ and Lacoss, 1968). More recent algorithms are efficient to detect and characterize continuous and global microbarom signals (Evers and Haak, 2001; Garcès, 2004; Landès et al., 2012; Hupe et al., 2018). The above mentioned studies were conducted using IMS infrasound data as well as infrasound records from national networks (e.g. KNMI network, Evers and Haak, 2001).

Seismic noise numerical simulations was introduced by Kedar et al. (Kedar et al., 2008). The good correlation between the observed microseism amplitudes and their predicted values according to the Longuett-Higgins theory was shown, demonstrating that microseism source locations can be tracked using numerical modeling (Shapiro, 2005; Shapiro and Campillo, 2004; Stehly et al., 2006; Stutzmann et al., 2012; Weaver, 2005).

Other studies were conducted to characterize the ambient infrasound noise. Garcès et al. (Garcés, 2004) compared one year of observed and modelled microbaroms for continuously measuring wind and temperature profiles in the low, middle and upper atmosphere. Smets et al. (2014) compared three months of microbarom observations with the expected values to study the life cycle of Sudden Stratospheric Warming events. Landès et al. (2014) compared the modelled source region with microbarom observations at operating IMS stations. Le Pichon et al. (2015) compared observations and modelling over a 7-month period to assess middle atmospheric wind and temperature models distributed by European Centre for Medium-Range Weather Forecasts (ECMWF). More recently, Hupe at al. (2018) showed a first order agreement between the modelled and observed

https://doi.org/10.5194/se-2020-8
Preprint. Discussion started: 3 March 2020

microbarom azimuth and amplitude in the North Atlantic. These agreements have been improved using more accurate wind profiles obtained from high resolution LIDAR middle atmospheric sounding.

In this paper, we further extend the approach developed by Hupe at al. (2018) using microbarom recorded by the dense Kazakhstani network. This network operated by the Institute of Geophysical Research (IGR) of the National Nuclear Center of the Republic of Kazakhstan includes not only infrasound but also seismic arrays.

To model microbarom signals, the WW3 wave action model developed by NOAA and distributed by IFREMER was used. For microseisms, the bathymetry strongly affects the source intensity (Ardhuin et al., 2011; Kedar et al., 2008); however, it has negligible impact on microbarom source strength (De Carlo et al., 2020). Microseisms propagate through the sea floor while microbaroms efficiently propagate at shallow propagation angles (e.g. incidence angles lower the 40° from the horizontal, typical of stratospheric and thermospheric propagation). Microbaroms are primarily affected by the temperature and wind structure of the atmosphere, whereas microseisms propagate through the static structureы of the solid Earth (Garcès, 2004). Therefore, the geometrical spreading and seismic attenuation are the main effects to account for microseism modelling (e.g. Kanamori and Given, 1981; Stutzmann et al., 2012), while the strong spatio-temporal variability of the middle atmosphere should be taken into account for microbarom modelling.

In the first part, we present the observation network and methods used in this study. In the second part, the processing and modelling results of microseism and microbarom signals recorded by the IGR seismo-acoustic network from 2014 to 2017. In the last part, comparisons between microbarom predictions and observed microbaroms and microseisms signals are discussed.

1 Observation network and methods

1.1 Observation network

The Kazakhstani seismo-acoustic network (KNDC, 2019) is unique for microbarom and microseism study, as it contains a five seismic and three infrasound arrays (Figure 1). Stations in the network are part of other global networks such as the IMS (CTBTO), IRIS consortium, etc. KNDC closely cooperates with the institutions responsible for these networks and leading seismic and infrasound centers such as the International Data Center (IDC, Austria) of the CTBTO, AFTAC and Commissariat à l'Energie Atomique (CEA, France).

The infrasound network consists of the IMS infrasound station IS31 located in north-west Kazakhstan (2.1 km aperture, 8 elements), two national arrays of 1 km aperture: KURIS (4 elements) in Kurchatov, MKIAR (9 elements), and in Makanchi village (Belyashov et al., 2013) (Figure 2). KURIS and MKIAR have been operating since 2010 and 2016, respectively. Microbarometers MB2000 and MB2005 are used at IS31 and KURIS, and Chaparral Physics microbarometers are installed at MKIAR. Figure 3Figure 3 shows the frequency response of the MB2000. The frequency responses of other sensors are flat from 0.01 to 5.0 Hz. Together with the IMS station IS46, these stations form a unique dense regional infrasound network.

https://doi.org/10.5194/se-2020-8
Preprint. Discussion started: 3 March 2020

Combining infrasound observables recorded by this network allows discriminating regional natural and anthropogenic sources (Smirnov, 2015; Smirnov et al., 2011, 2018).

The seismic network consists of Kurchatov Cross array and MKAR part of the IMS network, ABKAR and KKAR part of the Air Force Technical Applications Center (AFTAC, USA) network (Figure 1 and Table 1). The Kurchatov cross array differs from the others with 20 elements arranged as a cross with an aperture of 22 km (Figure 4). It consists of CMG-3V sensors. Although the 0.1-0.3 Hz frequency band is at the edge of the sensors frequency response, they can record microseisms. The configuration of ABKAR, BVAR, KKAR and MKAR are similar with nine elements and an aperture of ~5 km. ABKAR array configuration is shown in Figure 5Figure 5. These arrays are equipped with GS21 short period vertical sensors with flat response for frequencies above 1 Hz. Figure 6 shows the frequency response of GS-21 and CMG-3V sensors within the frequency range of 0.1-0.4 Hz. Surface waves from the ocean storms are well recorded by broad band seismometers. Body waves are also registered on GS21 short period sensors. Although, in the frequency band of interest (0.1-0.3 Hz), the signal attenuation is about 30 dB, all stations detect microseisms effectively due to their large amplitude above the background noise. A peculiarity of the network is that infrasound and seismic arrays are collocated at two sites (KURIS and Kurchatov Cross; MKIAR and MKAR) or installed relatively close to each other (IS31 and ABKAR are 220 km apart, Figure 1). With such setting, this network can be used to develop synergetic approaches to better constrain microbarom source and evaluate propagation effects.

1.2 Processing method

Microseisms are detected using the Progressive Multichannel Correlation Method (PMCC) (Cansi, 1995; Cansi and Klinger, 1997; Smirnov et al., 2011) in 10 linearly spaced frequency bands between 0.05 and 0.4 Hz. A fixed time window length of 200 s is used for each sub-band. For infrasound processing, the frequency band is broadened to 0.01-4 Hz using fifteen logarithmically scaled sub-bands, and time window length varying from 30 s to 200 s (Matoza et al., 2013). Only detections with a mean frequency ranging in the 0.1–0.4 Hz microbarom band are considered.

It is important to take into account uncertainties in azimuth and apparent velocity estimations identified in microbarom studies. The uncertainties of the estimated wave parameters of microseisms can be large due to the relatively small aperture of the seismic arrays. Uncertainties in wave parameter estimates are calculated considering the array geometry of the above mentioned infrasound and seismic arrays (Szuberla and Olson, 2004) (Table 1). For the infrasound arrays, the horizontal velocity is set to 340 m/s. For the seismic arrays, the value of 3000 m/s is chosen corresponding to the average speed of the Rayleigh wave. The uncertainties for the seismic arrays are significantly higher for the body waves due to higher velocities.

1.3 Source modelling

The microbarom source model is computed following the approach developed by De Carlo et al. (2018, 2020). Simulations are carried out using the microbarom generation theory, based on the non-linear oceanic wave interaction (Ardhuin and

https://doi.org/10.5194/se-2020-8
Preprint. Discussion started: 3 March 2020

125 Herbers, 2013). Input data are calculated over a global grid of resolution 0.5° in space and 6 hours in time. For the attenuation, we use a semi-empirical frequency dependent attenuation relation derived from massive parabolic equation simulations and consider realistic propagation scenario through the HRES IFS cycle 38r2 ECMWF atmospheric products (Le Pichon et al., 2012).

Atmospheric specifications are given at the station and are assumed to be constant along the propagation path. This approach
130 shows good results for microbaroms generated in the northern hemisphere similar to those described by De Carlo et al. (2018) and Hupe et al. (2018). However, such an approach does not explain the observed microbarom amplitude for sources located south of the stations. This discrepancy can be explained by the large propagation distance for which the assumed range independent atmosphere is no more valid, in particular, for sources located in the southern hemisphere where propagation involves upwind and downwind scenarios along the same path.

135 The correlation coefficient between the observed and predicted seasonal patterns is calculated following metrics elaborated by Landès (Landès et al., 2014). There are two different metrics: (i) S_{corr_Az} which defines the correlation between the observed (N_{obs}) and predicted (N_{pred}) marginal detection number in the direction θ_{Amax} versus time (t):

$$S_{corr\_Az} = C_{corr} [N_{obs} (\theta_{Amax}, t), N_{pred} (\theta_{Amax}, t)] \quad (1)$$

and (ii) S_{corr_Amp} for the correlation between the predicted and observed amplitude A_{max}.

140 $$S_{corr\_Amp} = C_{corr} [N_{obs} (A_{max}, t), N_{pred} (A_{max}, t)] \quad (2)$$

2 Results

2.1 Processing results

Signals from ocean storms recorded at infrasound and seismic arrays are successfully identified. Figure 7, Figure 8 and Figure
145 9 show the temporal variation of the azimuths of signals with maximum amplitudes extracted from the PMCC bulletins for each six-hour interval between 2014 and 2017. Figure 7 shows the results for station IS31.

In addition to these results, the expected microbarom parameters are also given. The graphs show pronounced seasonal variations for both azimuths and amplitudes. The largest amplitudes are observed during the winter months, when signals with azimuths of 320±20° prevail. Few detections with azimuths of 35±15° are also detected in winter. During the summer months,
150 low-frequency signals with azimuths of 210±50° dominate. In winter, the amplitudes range from ~0.001 to ~0.1 Pa, the largest values being observed in winter.

Figure 8 shows the observational data for KURIS. The azimuths measured at this station are similar to those recorded at IS31, with slightly higher values in winter (325±15°). In summer, two regimes are distinguished in the ranges azimuths 230±30° and 130±30°. Detections near 50° are also observed in winter. Similarly to IS31 data, KURIS data show that maximum microbarom
155 amplitudes are observed in winter. From summer to winter, the signal amplitude increases from 0.001 to 0.03 Pa.

https://doi.org/10.5194/se-2020-8
Preprint. Discussion started: 3 March 2020

MKIAR started recording microbaroms in August 2016 with repeatable seasonal variations (Figure 9). One detection system at 330±10° is observed in winter. In summer, two systems dominate: 230±25° and 110±25°.

As for microbaroms, microseism systems are extracted in the 0.1-0.4 Hz band within a six-hour interval time window from January 1, 2014, to December 31, 2017. Figure 10 shows the azimuths of low-frequency signals at four seismic IGR stations: (a) ABKAR, (b) KKAR, (c) Kurchatov Cross, and (d) MKAR stations. In winter, the graphs show similar features at all stations. A dominant detection system corresponds to signals from northwestern and northern directions. Other systems are identified: 340±15° (ABKAR), 350±25° (KKAR), 305±15° (Kurchatov Cross), and 320±10° and 5±5° (MKAR). In summer, the situation varies from one station to another. At ABKAR, one system at 290±15° is observed. At KKAR and MKAR, two systems with azimuths of 160±20°, 90±15° and 190±10°, 145±15°, respectively, are distinguished. Finally, at Kurchatov Cross array, it is impossible to identify a prevailing direction in summer. Figure 11 shows the maximum amplitudes at the four seismic arrays.

The seasonal trend of the maximum microseism amplitudes recorded at all seismic stations is similar, with a maximum observed in winter. At MKAR and KKAR, microseism amplitudes are characterized by a slight increase in the middle of summer. Such a peak is not observed at ABKAR. At the Kurchatov Cross station, there are a small amount of detections in summer. The graphs clearly show that the amplitudes vary synchronously even at smaller time scale (Figure 12). However, a decrease in amplitude is observed early January 2017 at all stations. As expected, the maximum amplitudes in winter decrease with increasing distance from the stations to the North Atlantic region (about 10, 8, and 4 nm/s for ABKAR, KKAR, and MKAR, respectively). At Kurchatov, the amplitude is significantly higher in winter (in the order of 80 nm/s).

2.2 Modelling results

Expected azimuths and amplitudes have been calculated for microbaroms recorded at IS31, KURIS, and MKIAR. Figure 7, Figure 8 and Figure 9 compare the observed and simulated arrivals at these stations. During winter months, a good agreement is found: IS31 records microbaroms with azimuths of 320±20° within the predicted range (Figure 7 a and c). A good agreement is also observed at KURIS (Figure 8 a, c) and MKIAR (Figure 9 a, c). During the summer months, the agreement in azimuths remains satisfactory at all stations. IS31 records microbaroms within 210±50° with a slight shift compared with the predicted system (185±50°). At KURIS, the observed systems 230±30° and 130±30° are different compared with the predicted ones (±10° and 160±10°). At MKIAR, during the summer months, microbaroms within the predicted range of 60-270° are consistent with the observed systems (230±25° and 110±25°). As the used source model was developed for microseisms (Ardhuin et al., 2011), an empirical scaling factor (F = 1:10000) must be applied for comparing the observed to the predicted amplitudes. At all stations, there is good agreement between the predicted and observed amplitudes during the winter months (Figure 7 d, Figure 8 d and Figure 9 d), but in summer the predicted amplitudes are overestimated when compared to the observed ones (Table 2).

To summarize, both amplitudes and azimuths are well predicted in winter as opposed to summer months. The observed discrepancies are explained here by unrealistic simulated signal attenuation for sources located in the southern hemisphere

https://doi.org/10.5194/se-2020-8
Preprint. Discussion started: 3 March 2020

which dominate in summer. Quantitative estimations of the prediction quality (S_{corr} calculated according to equations (1) and (2)) are summarized in Table 2.

3 Discussions

Where previous studies analysed microbarom signals at a single station (Hupe et al., 2018), further investigations are conducted in this study by considering a multi-year dataset of continuous records collected by the IGR network. Regional features of both microbaroms and microseisms are highlighted. Figure 13 shows the azimuthal distribution of infrasound detections with maximum amplitudes. Figure 14 shows similar histograms for seismic stations. One can distinguish seasonal trends for both infrasonic and seismic observations. In winter, microbaroms and microseisms are detected from northern and northwestern directions (Figure 13 b and Figure 14 b). In summer, southern, southwestern and southeastern directions dominate (Figure 13 c and Figure 14 c). However, signals from northwestern direction are also recorded at ABKAR, KKAR, and MKAR in summer. Azimuths differ from one station to another depending on the strongest microbarom and microseism source regions relative to the station locations. Observations and simulations show large temporal variations in the dominating microbarom source regions explained by the seasonal reversals of the prevailing stratospheric winds, which in turn, cause the migration of storm activity area to the winter hemisphere (Stutzmann et al., 2012). The histograms of the azimuthal distribution of microbaroms clearly show the dominating direction of arrivals in winter with prevailing directions ranging from 270 to 350° (Figure 13 b). The predicted azimuths are in good agreement with the observed ones (Figure 7 c, Figure 8 c, Figure 9 c, Figure 13 b and Table 2). During winter months, microseism observations exhibit a similar pattern with a larger spreading (250-360°), and an additional peak (0-20°) at KKAR and MKAR (Figure 14). These peaks are explained by body and seismic surface waves. At this stage, modelling the microseism source strength through the coupling with the bathymetry and the attenuation in the crust is necessary. Simulating microbaroms predicts signals mainly from a southern direction (180-200°). Such a peak is observed only at IS31 and MKAR. The closest peak observed at KURIS and MKIAR is shifted northwards by ~50°. The azimuths of the dominant cluster of detections are close to 90°. At MKIAR the peak is around 100°.

Thus, in winter, signals from ocean storms in the North Atlantic region dominate at all stations. This is supported by the simulation results which account for the predicted source regions and propagation effects. However, during summer months, stations detect unpredicted signals from southern regions. In this study, the method used to predict the attenuation assumes a range independent atmosphere along the propagation path. Such an approach cannot be applied to situations involving long propagation ranges, where significant along-path variability of wind and temperature profiles may occur (especially when sources and network are located in different hemispheres).

Using historical IGR datasets, the spatiotemporal variability of microbarom signals due to changes in the source location and the structure of the atmospheric waveguides can be studied. There is a clear seasonal trend in the directions and amplitudes of microbaroms and microseisms (Figure 7, Figure 8 and Figure 9). Moreover, it is shown that the microseism amplitudes

https://doi.org/10.5194/se-2020-8
Preprint. Discussion started: 3 March 2020

synchronously vary at all stations (Figure 11 and Figure 12). A similar pattern is shown for microbaroms (Figure 15). A better agreement between observations and simulations is found for the azimuths.

As already shown by Evers and Siegmund (2009) and Smets and Evers (Smets and Evers, 2014), the life cycle of SSW events can be inferred from the observed spatio-temporal variations of microbarom parameters. Such observations are noted at IS31 where microbaroms in early and late February 2017 shifted to easterly directions (~40°) consistent with the simulated source regions in the Northern Pacific (Figure 7). As noted for IS31, KURIS also recorded signals with azimuths of ~40° in late January 2017 (Figure 8). Similarly, signals from ~100° were also recorded during the 2017 SSW event at MKIAR. However, the observed azimuths differ from those expected (~60°). It is likely that this station recorded signals from other regions over the Pacific Ocean not described by the ocean wave model, or inaccuracy in the used ECMWF products (Blanc et al., 2018).

These findings are consistent with comparisons between the observed and modelled microbarom signals carried out by Landès (Landès et al., 2014) at IS31. This study shows that modelling well describes microbarom sources in the North Atlantic in winter and poorly explains signals in summer. This mismatch can be explained by the interference of permanent natural or anthropogenic sources overlapping microbarom signals in the same frequency band. These sources could be mining explosions (Hagerty et al., 2002), subsonic (Evers, 2005) or supersonic aircrafts (Donn, 1978; Liszka and Waldemark, 1995), as well as auroral infrasound (Wilson, 1971).

Conclusions

The IGR seismo-acoustic network is much denser than the global IMS infrasound network. Therefore, analyzing multi-year archives of continuous recordings yields additional information about the spatial and temporal variability of the ambient noise originating from two hemispheres. In winter, the most intense oceanic storms are modelled in the Northern Atlantic, and their signature prevails on infrasound and seismic records. When SSW events occur, abrupt changes in the stratospheric wind direction allow signals from the North Pacific to be detected by infrasound stations. Simulated and observed microbarom parameters are consistent, as shown by high correlation coefficients. The largest amplitudes of both microbaroms and microseisms are found for sources in the Northern Atlantic. Exploiting the synergy between seismic and infrasound ambient noise observations is thus valuable to: (i) better constrain the source location as azimuthal errors at the seismic ABKAR, KKAR and MKAR arrays that are approximately 10 times larger than at IS31, and MKIAR due to shorter wavelength; (ii) improve the detectability of ocean-wave interaction, and location accuracy as microbarom wave parameters are less affected by heterogeneities in the propagation medium, and; (iii) improve the physical description of seismo-acoustic energy partitioning at the ocean-atmosphere interface.

Additional studies are required to further evaluate whether the bathymetry effect could explain discrepancies between the observed microbarom and microseism signals (Longuet-Higgins, 1950; Stutzmann et al., 2012, De Carlo 2020). In summer, the microbarom and microseism sources which dominate in the southern hemisphere more especially along the peri-antarctic belt are likely at the origin of the weak signals observed south of the IGR network. For such long propagation ranges, numerical

https://doi.org/10.5194/se-2020-8
Preprint. Discussion started: 3 March 2020

simulation using range dependent atmosphere models could reduce the difference between the observed and modelled amplitude. Including additional data from other seismo-acoustic network in the southern hemisphere would help validating long-range propagation modelling, better characterize station-specific ambient noise signatures, and enhance discrimination methods at a regional scale.

Code/Data availability

Atmospheric wind and temperature profiles are derived from operational high-resolution atmospheric model analysis, defined by the Integrated Forecast System of the ECMWF, available at https://www.ecmwf.int/ (last access: 2 September 2019; ECMWF, 2018). Waveform data for the seismic and infrasound arrays of the CTBTO IMS (https://www.ctbto.org/, last access: 2 September 2019) used in this study are available to the authors, being members of National Data Centers for the CTBTO. Data of the Kazakhstani national seismic and infrasound arrays are available under request from the Institute of Geophysical Researches, National Nuclear Center of Kazakhstan. Results of the microseism and microbarom detections by the seismo-acoustic Kazakh network and of the microbarom simulation for the infrasound arrays of the network are available at ISC repository (Smirnov et al., 2020).

Author contribution

N. Shapiro and A. Le Pichon suggested main outlines of the paper. A. Smirnov and A. Le Pichon prepared historical dataset for processing. M. De Carlo and A. Le Pichon developed the microbarom source model. A. Smirnov performed microbarom and microseism detections and propagation simulations. A. Smirnov prepared the manuscript with contributions from all co-authors. A. Le Pichon, M. De Carlo and S. Kulichkov made critical reviews and comments to improve the manuscript.

Competing interests

The authors declare that they have no conflict of interest.

Acknowledgements

This research has been supported by the Commissariat a` l'Energie Atomique (CEA, France). The work of NS has been supported by the European Research Council (ERC) under the European Union Horizon 2020 Research and Innovation Programme (grant agreement 787399-SEISMAZE), the Russian Ministry of Education and Science (grant N 14.W03.31.0033) and Russian Foundation for Basic Research (project no. 18-05-00576). Authors also thank Anna Smirnova for the help in the manuscript preparation.

References

Ardhuin, F. and Herbers, T. H. C.: Noise generation in the solid Earth, oceans and atmosphere, from nonlinear interacting surface gravity waves in finite depth, J. Fluid Mech., 716, 316–348, doi:10.1017/jfm.2012.548, 2013.

Ardhuin, F., Stutzmann, E., Schimmel, M. and Mangeney, A.: Ocean wave sources of seismic noise, J. Geophys. Res., 116(C9), doi:10.1029/2011jc006952, 2011.

https://doi.org/10.5194/se-2020-8
Preprint. Discussion started: 3 March 2020

Belyashov, A., Dontsov, V., Dubrovin, V., Kunakov, V. and Smirnov, A.: New infrasound array "Kurchatov", NNC RK Bull., (2), 24–30, 2013.

Blanc, E., Pol, K., Le Pichon, A., Hauchecorne, A., Keckhut, P., Baumgarten, G., Hildebrand, J., Höffner, J., Stober, G., Hibbins, R., Espy, P., Rapp, M., Kaifler, B., Ceranna, L., Hupe, P., Hagen, J., Rüfenacht, R., Kämpfer, N. and Smets, P.: Middle Atmosphere Variability and Model Uncertainties as Investigated in the Framework of the ARISE Project, Infrasound Monit. Atmos. Stud., 845–887, doi:10.1007/978-3-319-75140-5_28, 2018.

Cansi, Y.: An automatic seismic event processing for detection and location: The P.M.C.C. Method, Geophys. Res. Lett., 22(9), 1021–1024, doi:10.1029/95gl00468, 1995.

Cansi, Y. and Klinger, Y.: An Automated Data Processing Method for Mini-Arrays, Newsl. Eur. Seismol. Cent., 1021–1024, 1997.

Capon, J.: Long-Period Signal Processing Results for LASA, NORSAR and ALPA, Geophys. J. Int., 31(1–3), 279–296, doi:10.1111/j.1365-246x.1972.tb02370.x, 1972.

De Carlo, M., Le Pichon, A., Ardhuin, F. and Näsholm, S.: Characterizing and modelling ocean ambient noise using infrasound network and middle atmospheric models, NNC RK Bull., (2), 144–151, 2018.

De Carlo, M., Ardhuin, F. and Le Pichon, A.: Atmospheric infrasound radiation from ocean waves in finite depth: a unified generation theory and application to radiation patterns, J. Acoust. Am., In review, 2019.

Ceranna, L., Matoza, R., Hupe, P., Le Pichon, A. and Landès, M.: Systematic Array Processing of a Decade of Global IMS Infrasound Data, Infrasound Monit. Atmos. Stud., 471–482, doi:10.1007/978-3-319-75140-5_13, 2018.

Donn, W. L.: Exploring the atmosphere with sonic booms, Am. Sci., 66, 724–733, 1978.

Evers, L. G.: Infrasound monitoring in the Netherlands, J. Netherlands Acoust. Soc. (Nederlands Akoestisch Genoot., 176, 1–11, 2005.

Evers, L. G. and Haak, H. W.: Listening to sounds from an exploding meteor and oceanic waves, Geophys. Res. Lett., 28(1), 41–44, doi:10.1029/2000gl011859, 2001.

Evers, L. G. and Siegmund, P.: Infrasonic signature of the 2009 major sudden stratospheric warming, Geophys. Res. Lett., 36(23), doi:10.1029/2009gl041323, 2009.

Garcés, M.: On using ocean swells for continuous infrasonic measurements of winds and temperature in the lower, middle, and upper atmosphere, Geophys. Res. Lett., 31(19), doi:10.1029/2004gl020696, 2004.

Hagerty, M. T., Kim, W.-Y. and Martysevich, P.: Infrasound Detection of Large Mining Blasts in Kazakstan, Pure Appl. Geophys., 159(5), 1063–1079, doi:10.1007/s00024-002-8673-3, 2002.

Hasselmann, K.: A statistical analysis of the generation of microseisms, Rev. Geophys., 1(2), 177, doi:10.1029/rg001i002p00177, 1963.

Hasselmann, K.: Feynman diagrams and interaction rules of wave-wave scattering processes, Rev. Geophys., 4(1), 1, doi:10.1029/rg004i001p00001, 1966.

Haubrich, R. A. and McCamy, K.: Microseisms: Coastal and pelagic sources, Rev. Geophys., 7(3), 539,

doi:10.1029/rg007i003p00539, 1969.

Hupe, P., Ceranna, L., Pilger, C., de Carlo, M., Le Pichon, A., Kaifler, B. and Rapp, M.: Assessing middle atmosphere weather models using infrasound detections from microbaroms, Geophys. J. Int., 216(3), 1761–1767, doi:10.1093/gji/ggy520, 2018.

IFREMER: Wave Watch 3, [online] Available from: ftp://ftp.ifremer.fr/ifremer/ww3/ (Accessed 3 October 2018), 2018.

Kanamori, H. and Given, J. W.: Use of long-period surface waves for rapid determination of earthquake-source parameters, Phys. Earth Planet. Inter., 27(1), 8–31, doi:10.1016/0031-9201(81)90083-2, 1981.

Kedar, S., Longuet-Higgins, M., Webb, F., Graham, N., Clayton, R. and Jones, C.: The origin of deep ocean microseisms in the North Atlantic Ocean, Proc. R. Soc. A Math. Phys. Eng. Sci., 464(2091), 777–793, doi:10.1098/rspa.2007.0277, 2008.

KNDC: Observation network of the Institute of Geophysical Researches of the National Nuclear Center of the Republic of Kazakhstan., [online] Available from: http://www.kndc.kz/index.php?option=com_content&view=article&id=45&Itemid=147&lang=en (Accessed 3 October 2019), 2019.

Landès, M., Ceranna, L., Le Pichon, A. and Matoza, R. S.: Localization of microbarom sources using the IMS infrasound network, J. Geophys. Res. Atmos., 117(D6), n/a-n/a, doi:10.1029/2011jd016684, 2012.

Landès, M., Le Pichon, A., Shapiro, N. M., Hillers, G. and Campillo, M.: Explaining global patterns of microbarom observations with wave action models, Geophys. J. Int., 199(3), 1328–1337, doi:10.1093/gji/ggu324, 2014.

Liszka, L. and Waldemark, K.: High Resolution Observations of Infrasound Generated by the Supersonic Flights of Concorde, J. Low Freq. Noise, Vib. Act. Control, 14(4), 181–192, doi:10.1177/026309239501400403, 1995.

Longuet-Higgins, M. S.: A Theory of the Origin of Microseisms, Philos. Trans. R. Soc. A Math. Phys. Eng. Sci., 243(857), 1–35, doi:10.1098/rsta.1950.0012, 1950.

Matoza, R. S., Landès, M., Le Pichon, A., Ceranna, L. and Brown, D.: Coherent ambient infrasound recorded by the International Monitoring System, Geophys. Res. Lett., 40(2), 429–433, doi:10.1029/2012gl054329, 2013.

Olson, J. V and Szuberla, C. A. L.: Distribution of wave packet sizes in microbarom wave trains observed in Alaska, J. Acoust. Soc. Am., 117(3), 1032–1037, doi:10.1121/1.1854651, 2005.

Le Pichon, A., Ceranna, L. and Vergoz, J.: Incorporating numerical modeling into estimates of the detection capability of the IMS infrasound network, J. Geophys. Res. Atmos., 117(D5), n/a-n/a, doi:10.1029/2011jd016670, 2012.

Le Pichon, A., Assink, J. D., Heinrich, P., Blanc, E., Charlton-Perez, A., Lee, C. F., Keckhut, P., Hauchecorne, A., Rüfenacht, R., Kämpfer, N., Drob, D. P., Smets, P. S. M., Evers, L. G., Ceranna, L., Pilger, C., Ross, O. and Claud, C.: Comparison of co-located independent ground-based middle atmospheric wind and temperature measurements with numerical weather prediction models, J. Geophys. Res. Atmos., 120(16), 8318–8331, doi:10.1002/2015jd023273, 2015.

Shapiro, N. M.: High-Resolution Surface-Wave Tomography from Ambient Seismic Noise, Science (80-.)., 307(5715), 1615–1618, doi:10.1126/science.1108339, 2005.

Shapiro, N. M. and Campillo, M.: Emergence of broadband Rayleigh waves from correlations of the ambient seismic noise, Geophys. Res. Lett., 31(7), n/a-n/a, doi:10.1029/2004gl019491, 2004.

https://doi.org/10.5194/se-2020-8
Preprint. Discussion started: 3 March 2020

Smets, P. S. M. and Evers, L. G.: The life cycle of a sudden stratospheric warming from infrasonic ambient noise observations, J. Geophys. Res. Atmos., 119(21), 12,12-84,99, doi:10.1002/2014jd021905, 2014.

Smirnov, A.: The Variety Of Infrasound Sources Recorded By Kazakhstani Stations, in CTBT: Science and Technology, Vienna. [online] Available from: https://www.ctbto.org/fileadmin/user_upload/SnT2015/SnT2015_Posters/T2.3-P20.pdf, 2015.

Smirnov, A., Dubrovin, V., Evers, L. G. and Gibbons, S. J.: Explanation of the nature of coherent low-frequency signal sources recorded by the monitoring station network of the NNC RK, in CTBT: Science and Technology 2011. [online] Available from: https://www.ctbto.org/fileadmin/user_upload/SandT_2011/posters/T4-P12 A_Smirnov Explanation of the nature of coherent low-frequency signal sources recorded by the monitoring station.pdf, 2011.

Smirnov, A., de Carlo, M., Le Pichon, A. and Shapiro, N. M.: Signals from severe ocean storms in North Atlantic as it detected in Kazakhstan: observations and modelling, NNC RK Bull., (2), 152–160, 2018.

Smirnov, A., De Carlo, M., Le Pichon, A., Shapiro, N. and Kulichkov, S.: Results of the microseism and microbarom detections by the seismo-acoustic Kazakh network and of the microbarom simulation for the infrasound arrays of the network, Results microseism microbarom Detect. by Seism. Kazakh Netw. microbarom Simul. infrasound arrays Netw., doi:10.31905/dsw7l5bv, 2020.

Stehly, L., Campillo, M. and Shapiro, N. M.: A study of the seismic noise from its long-range correlation properties, J. Geophys. Res., 111(B10), doi:10.1029/2005jb004237, 2006.

Stutzmann, E., Ardhuin, F., Schimmel, M., Mangeney, A. and Patau, G.: Modelling long-term seismic noise in various environments, Geophys. J. Int., 191(2), 707–722, doi:10.1111/j.1365-246x.2012.05638.x, 2012.

Szuberla, C. A. L. and Olson, J. V: Uncertainties associated with parameter estimation in atmospheric infrasound arrays, J. Acoust. Soc. Am., 115(1), 253–258, doi:10.1121/1.1635407, 2004.

ToksoZ, M. N. and Lacoss, R. T.: Microseisms: Mode Structure and Sources, Science (80-.)., 159(3817), 872–873, doi:10.1126/science.159.3817.872, 1968.

Waxler, R. and Gilbert, K. E.: The radiation of atmospheric microbaroms by ocean waves, J. Acoust. Soc. Am., 119(5), 2651–2664, doi:10.1121/1.2191607, 2006.

Weaver, R. L.: GEOPHYSICS: Information from Seismic Noise, Science (80-.)., 307(5715), 1568–1569, doi:10.1126/science.1109834, 2005.

Wilson, C. R.: Auroral infrasonic waves and poleward expansions of auroral substorms at Inuvik, N.W.T., Canada, Geophys. J. R. astr. Soc., 26, 179–181, 1971.

https://doi.org/10.5194/se-2020-8
Preprint. Discussion started: 3 March 2020

Solid Earth
Discussions
Open Access
EGU

385

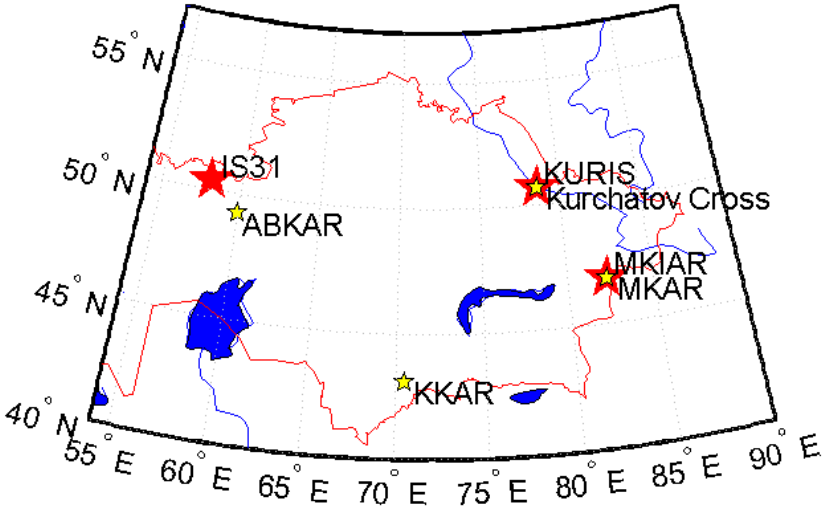

390 **Figure 1.** **IGR monitoring network. Yellow and red stars are seismic and infrasound arrays, respectively. Seismic and infrasound arrays are collocated at two sites. IS31 infrasound and ABKAR seismic arrays are located 200 km apart.**

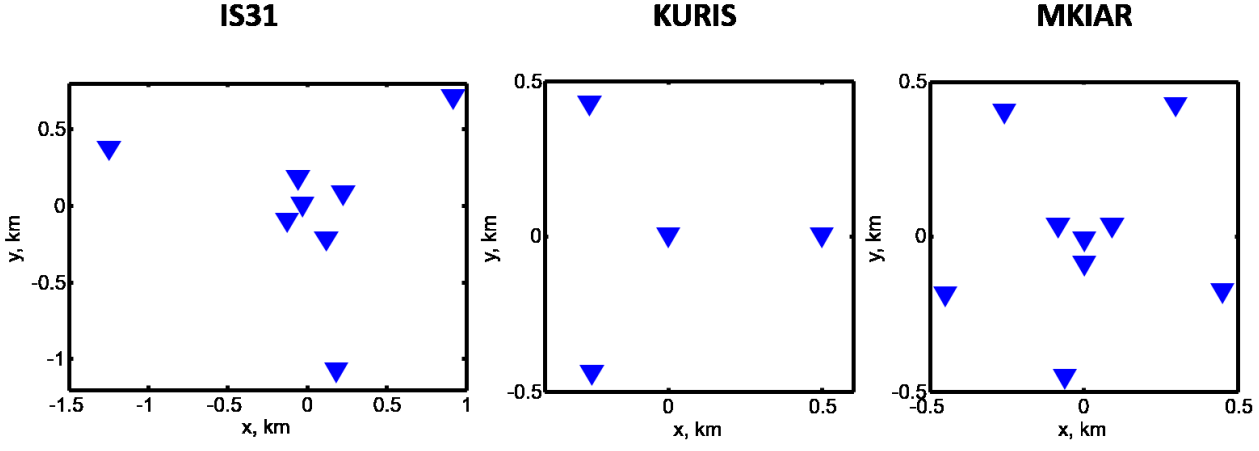

Figure 2. **Infrasound arrays of the IGR monitoring network: IS31 (2 km aperture), KURIS and MKIAR (1 km aperture).**

https://doi.org/10.5194/se-2020-8
Preprint. Discussion started: 3 March 2020

Solid Earth
Discussions
Open Access
EGU

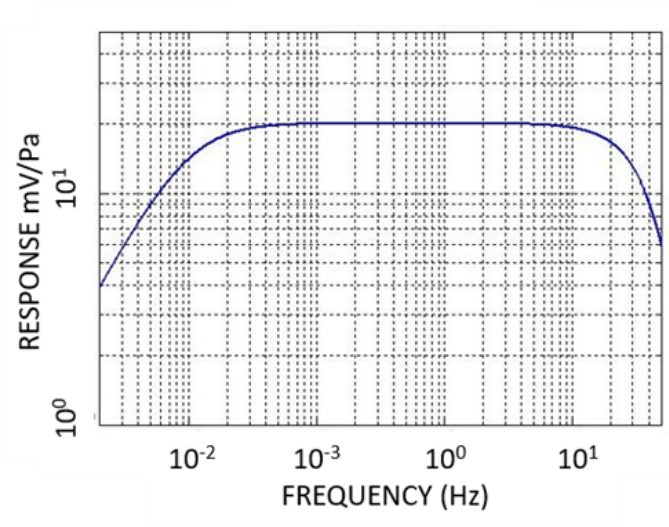

395

Figure 3. **Frequency response of the MB2000 microbarometer.**

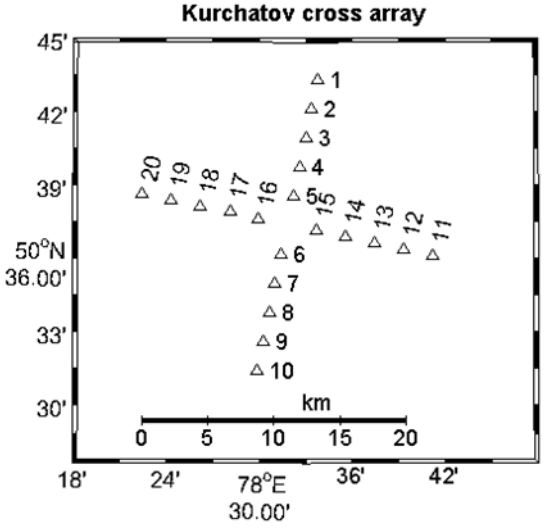

Figure 4. **Configuration of the Kurchatov Cross seismic array.**

400

https://doi.org/10.5194/se-2020-8
Preprint. Discussion started: 3 March 2020

Solid Earth
Discussions
Open Access
EGU

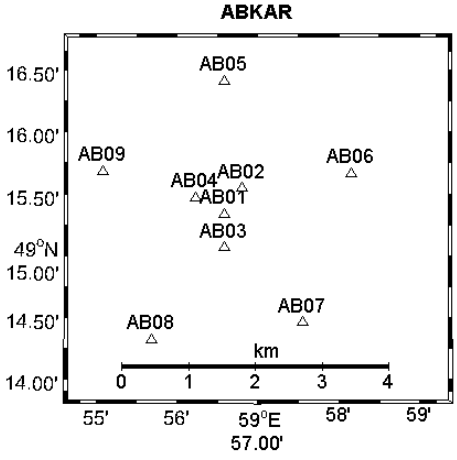

Figure 5. **Configuration of the ABKAR seismic array which includes h a central point, inner and outer circles of 3 and 5 elements, respectively.**

405

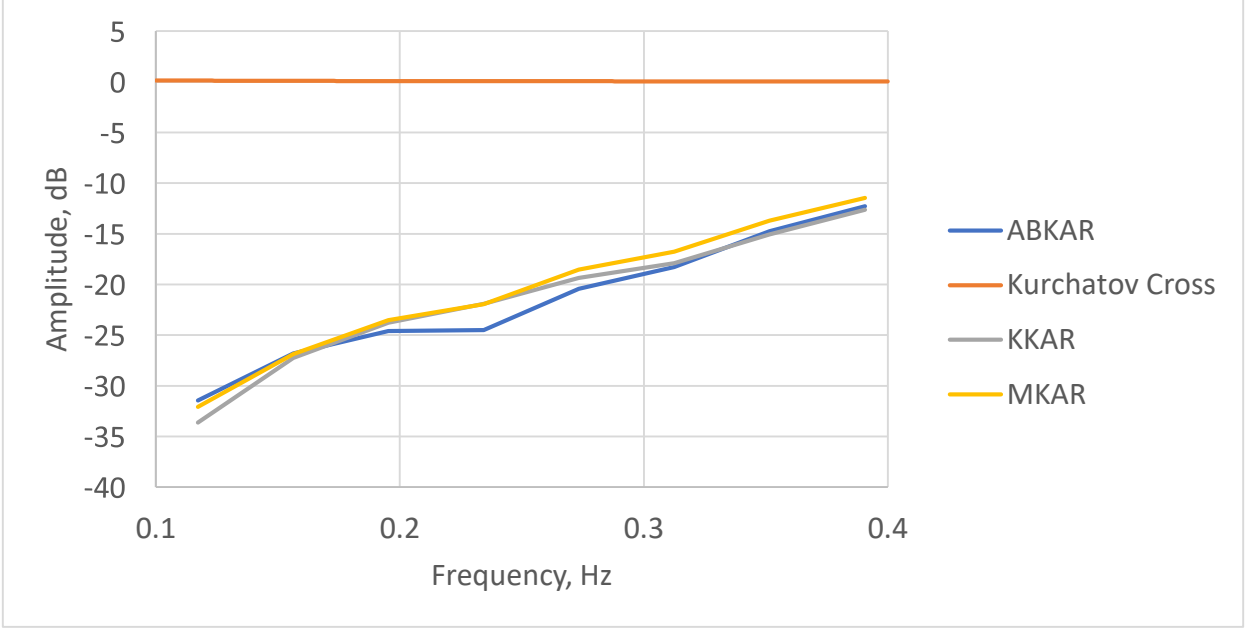

Figure 6. **Frequency response of GS-21 at ABKAR, KKAR and MKAR and CMG-3V at the Kurchatov Cross array between 0.1 and 0.4 Hz.**

410

https://doi.org/10.5194/se-2020-8
Preprint. Discussion started: 3 March 2020

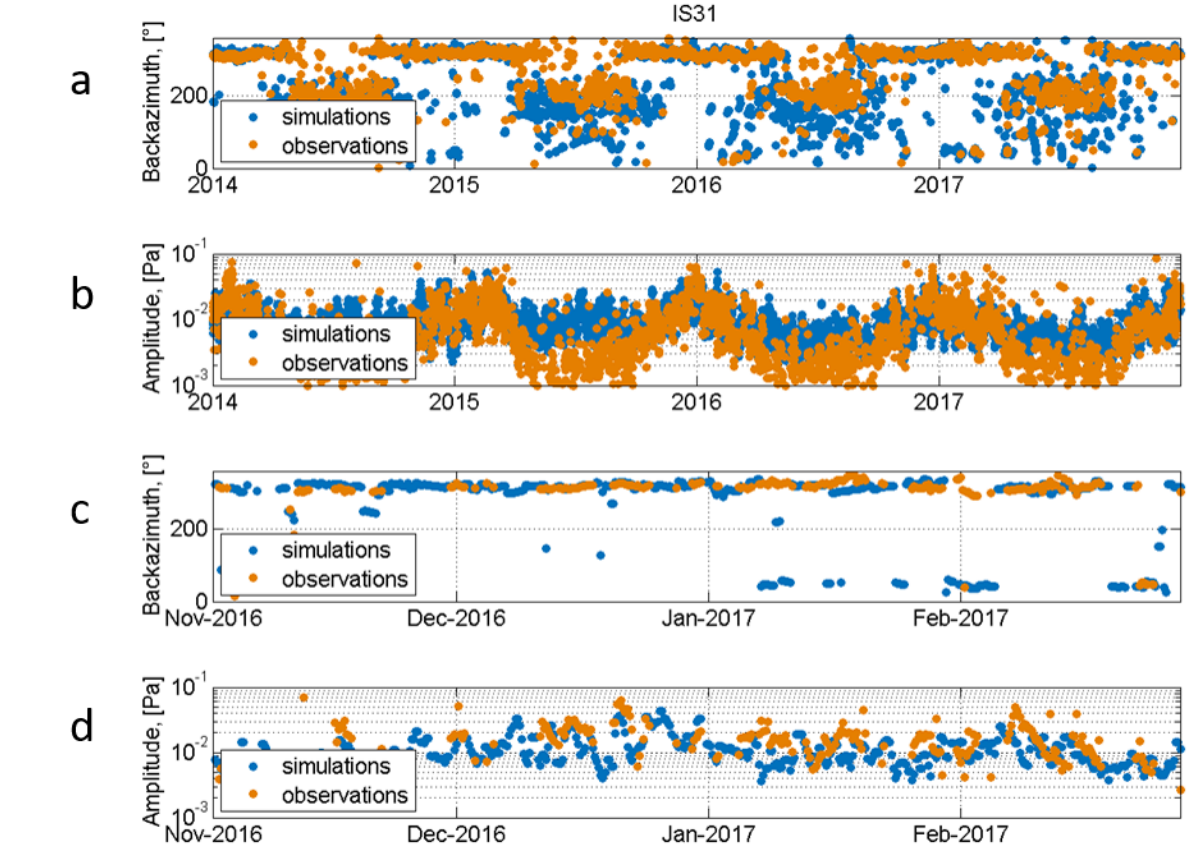

415 **Figure 7. Dominant amplitude and azimuth of infrasound signals at IS31 with a time resolution of 6 hours from 1 January 1, 2014 to December 31, 2017 (orange circles). Blue circles denote simulated values. (c) and (d): detail from November 1, 2016, to February 28, 2017.**

https://doi.org/10.5194/se-2020-8
Preprint. Discussion started: 3 March 2020

Solid Earth
Discussions
Open Access
EGU

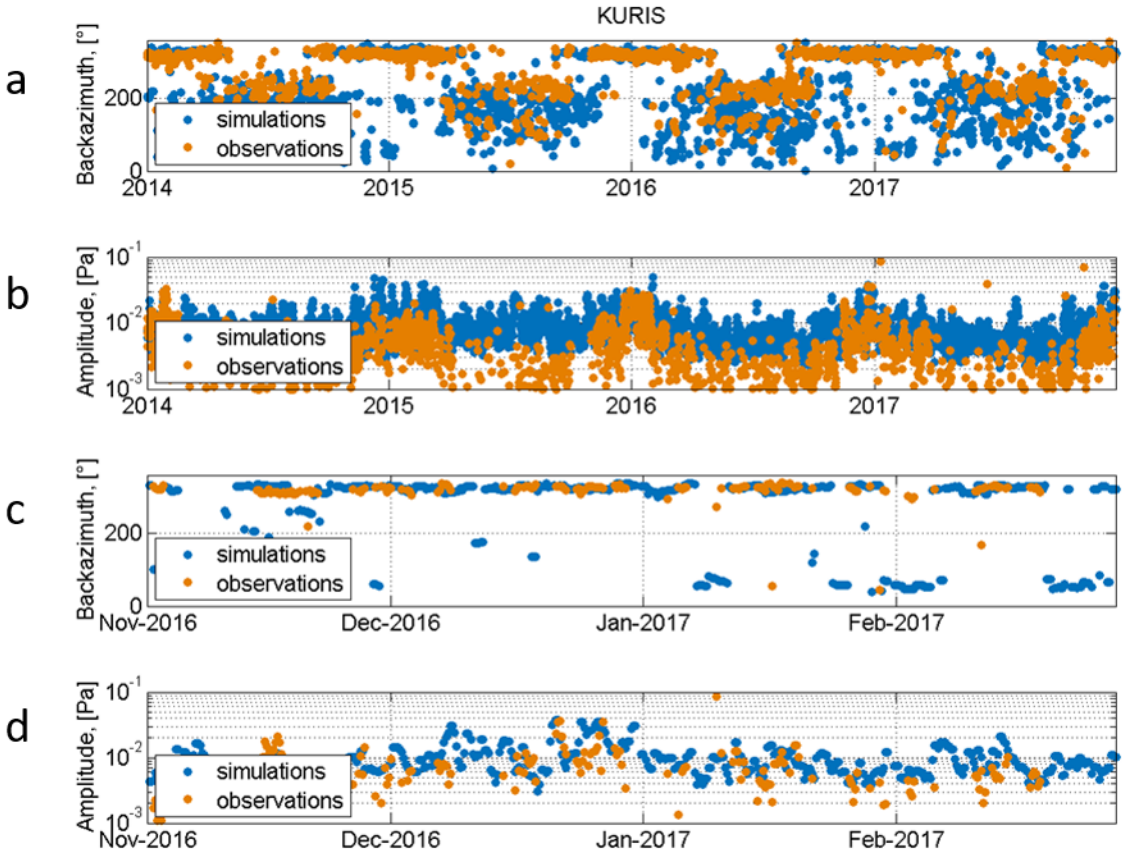

420 **Figure 8.** **Same as Figure 7 for KURIS every from 1 January 1, 2014 to December 31, 2017.**

https://doi.org/10.5194/se-2020-8
Preprint. Discussion started: 3 March 2020

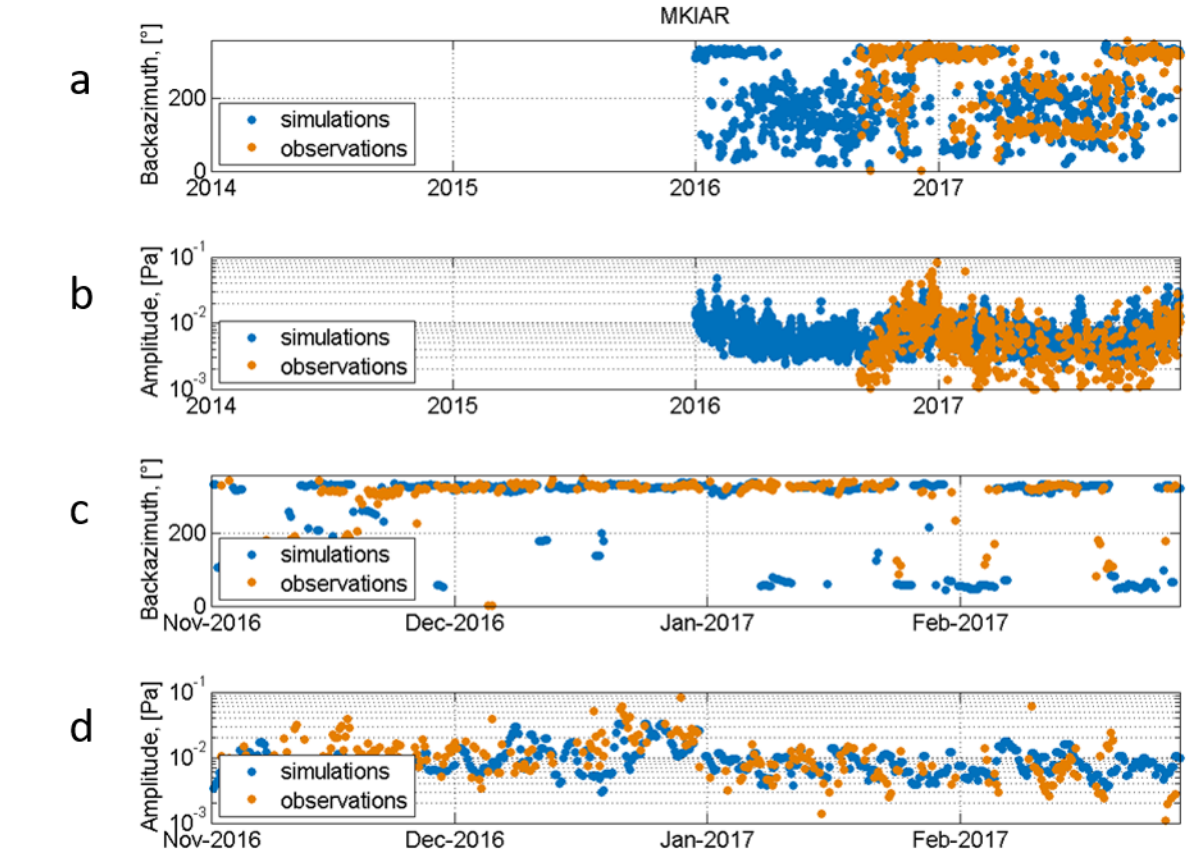

Figure 9. **Same as Figure 7 for MKIAR from 1 January 1, 2014 to December 31, 2017.**

https://doi.org/10.5194/se-2020-8
Preprint. Discussion started: 3 March 2020

Solid Earth
Discussions
Open Access
EGU

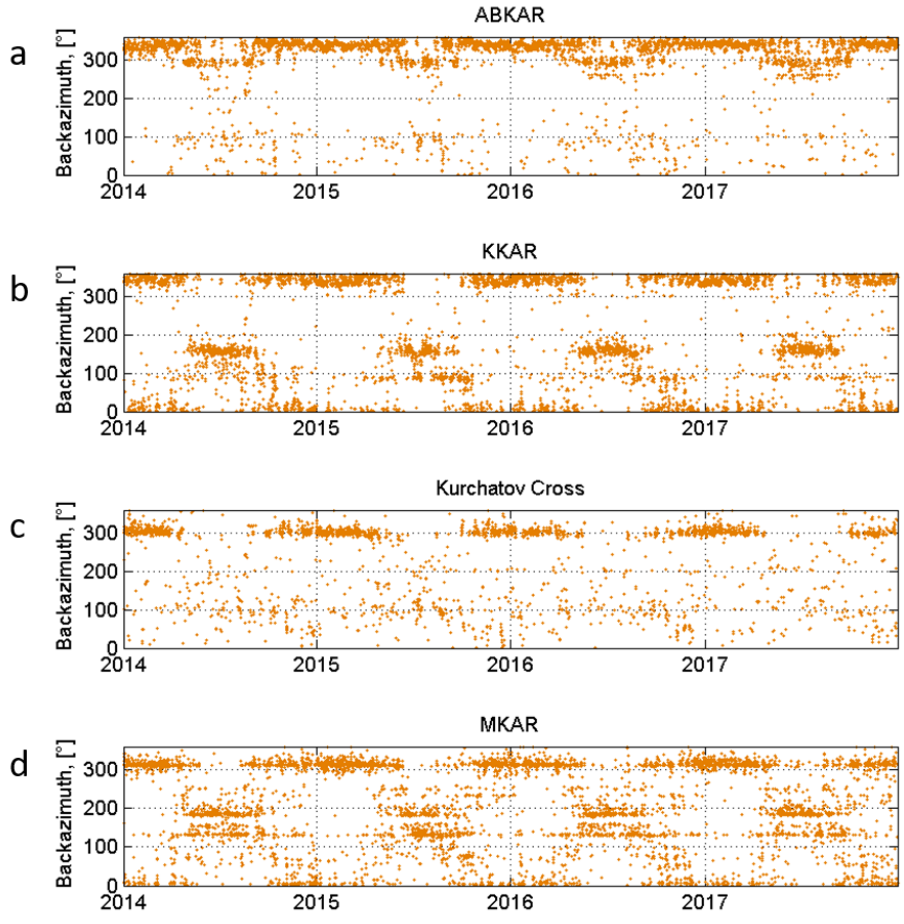

425

Figure 10. Dominant azimuth of seismic signals in the 0.1-0.4 Hz band detected at ABKAR (a), KKAR (b), Kurchatov Cross (c), and MKAR (d) arrays from January, 1 2014 to December 31, 2017.

https://doi.org/10.5194/se-2020-8
Preprint. Discussion started: 3 March 2020

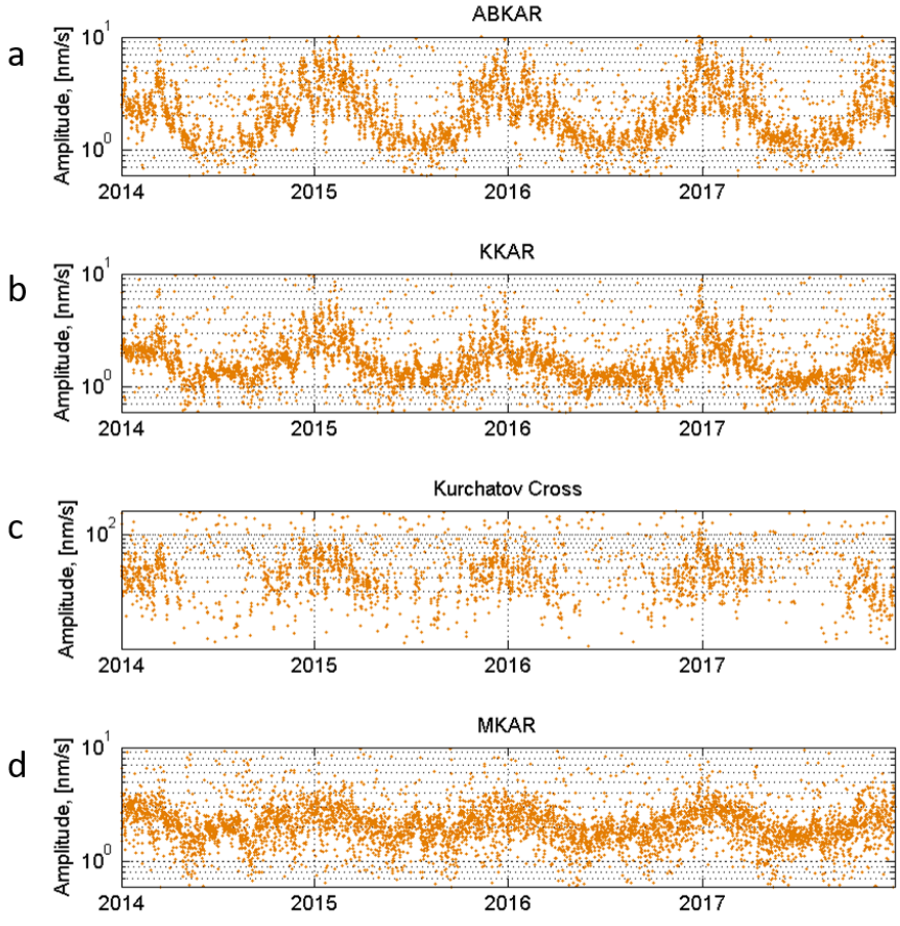

Figure 11. Dominant amplitude of seismic signals in the 0.1-0.4 Hz band detected at ABKAR (a), KKAR (b), Kurchatov Cross array (c), and MKAR (d) arrays from January, 1 2014 to December 31, 2017.

https://doi.org/10.5194/se-2020-8
Preprint. Discussion started: 3 March 2020

Solid Earth
Discussions
Open Access
EGU

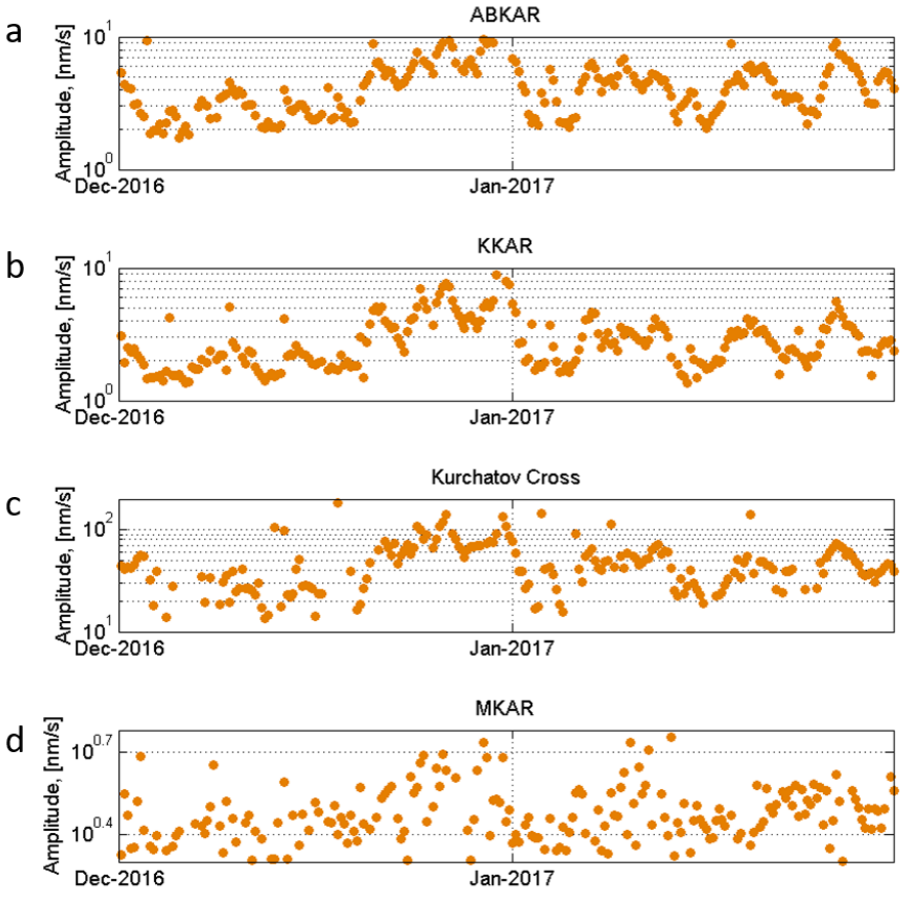

Figure 12. Dominant amplitude of seismic signals in the 0.1-0.4 Hz band detected at ABKAR (a), KKAR (b), Kurchatov Cross array (c), and MKAR (d) arrays from December 1, 2016 to January 31, 2017.

https://doi.org/10.5194/se-2020-8
Preprint. Discussion started: 3 March 2020

Solid Earth
Discussions
Open Access
EGU

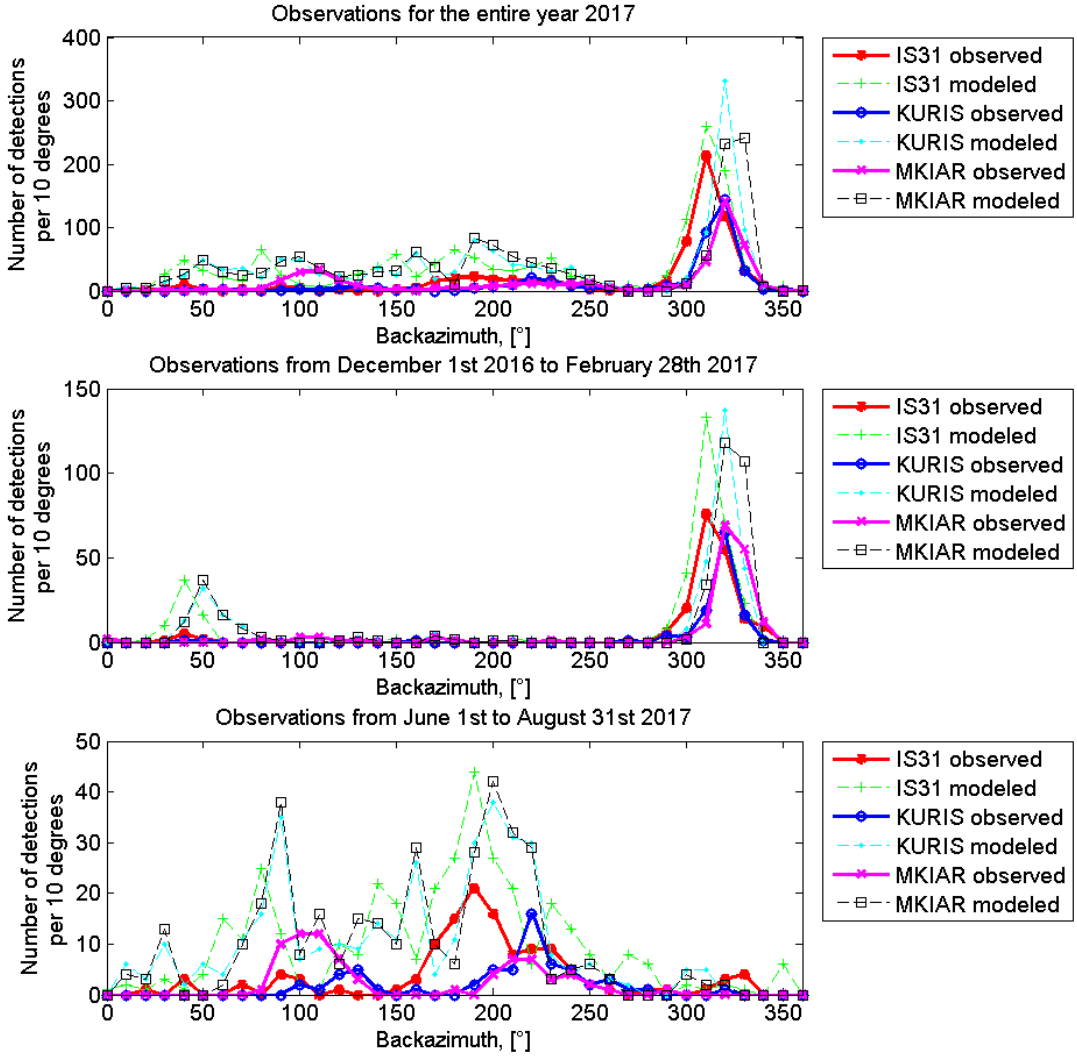

Figure 13. **Azimuthal distribution of detections with maximum amplitudes for infrasound stations throughout 2017 (a), from December 1, 2016, to February 28, 2017 (b), and from June 1 to August 31, 2017 (c).**

https://doi.org/10.5194/se-2020-8
Preprint. Discussion started: 3 March 2020

Solid Earth
Discussions
Open Access
EGU

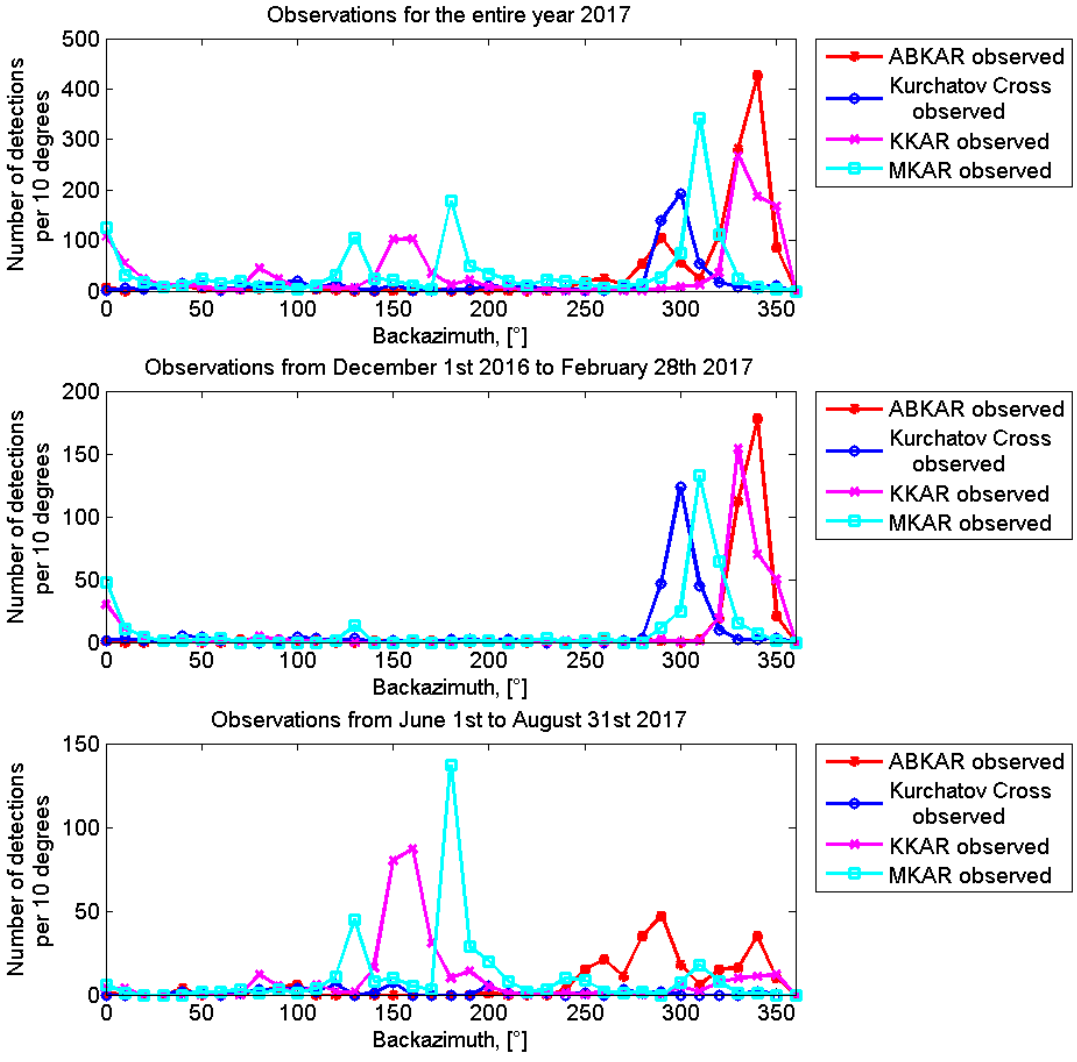

Figure 14. Azimuthal distribution of detections with maximum amplitudes for seismic stations throughout 2017 (a), from December 1, 2016, to February 28 (b), 2017, and from June 1 to August 31, 2017 (c).

445

https://doi.org/10.5194/se-2020-8
Preprint. Discussion started: 3 March 2020

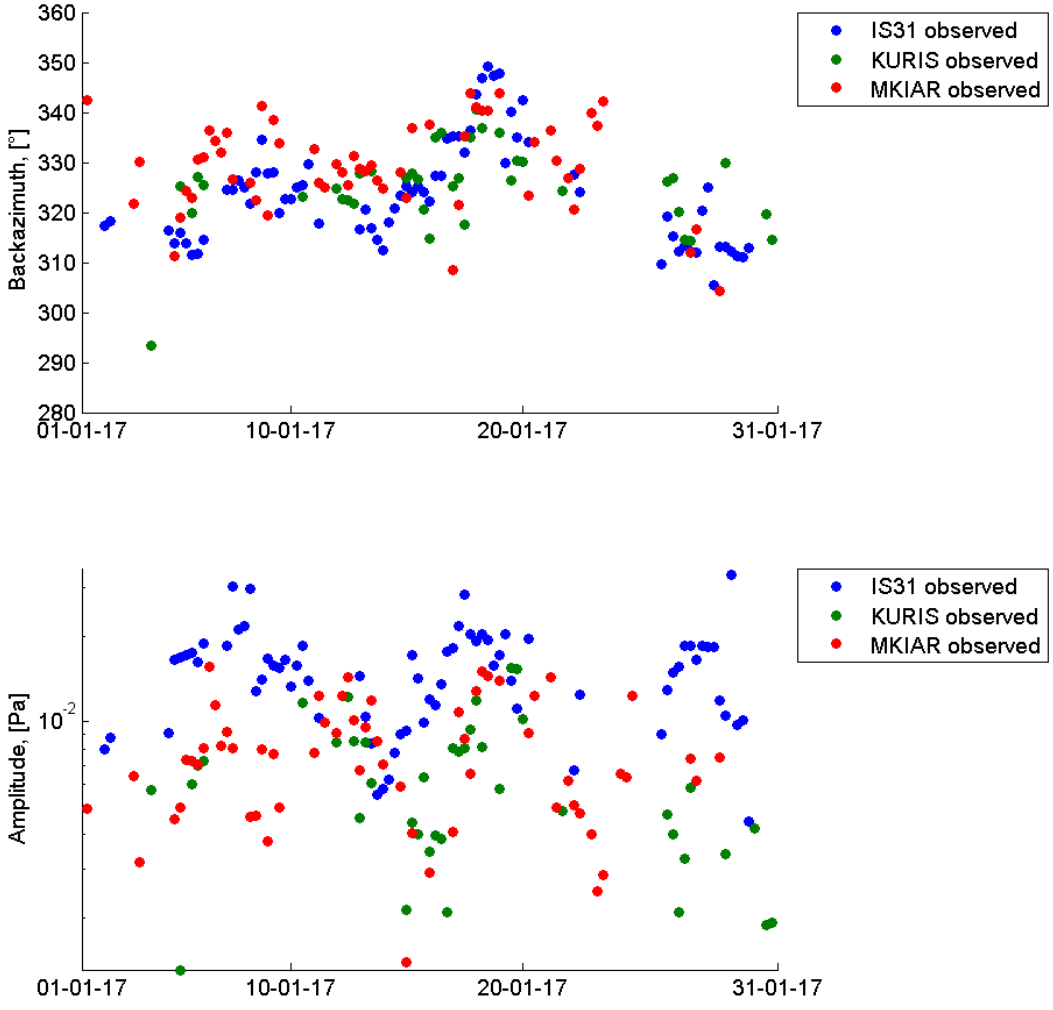

Figure 15. Spatio-temporal variations of microbarom parameters recorded at IS31, KURIS, and MKIAR. Azimuth (top) and amplitude (bottom) variations during January 2017.

Table 1. Uncertainties of azimuth and apparent velocity estimates.

Parameter	Horizontal velocity, m/s	IS31	KURIS	MKIAR	ABKAR	KKAR	MKAR	Kurchatov Cross
δΘ (°)	340	0.55 - 0.74	2.05 – 2.34	0.58 - 0.67				
δV (m/s)		3.8 – 4.4	12 - 14	3.5 – 3.9				

https://doi.org/10.5194/se-2020-8
Preprint. Discussion started: 3 March 2020

δΘ (°)	3000				4.89 – 5.64	5.14 – 6.30	4.55 – 6.84	0.48 – 0.49
δV (m/s)					250 – 290	270 – 330	220 - 380	25 – 26

450

Table 2. Estimations of the prediction quality for microbarom amplitudes and azimuths.

Station	Long-term Observation period	S_{corr_Az}	S_{corr_Amp}	Observation period on winter	S_{corr_Az}	S_{corr_Amp}	Observation period on summer	S_{corr_Az}	S_{corr_Amp}
IS31	2014 - 2017	0.61	0.39	Dec 2016 – Feb 2017	0.76	0.53	Jun 2017 – Aug 2017	0.44	0.26
KURIS	2014 - 2017	0.52	0.23	Dec 2016 – Feb 2017	0.82	0.58	Jun 2017 – Aug 2017	0.16	0.18
MKIAR	Sep 2016 – Dec 2017	0.62	0.5	Dec 2016 – Feb 2017	0.82	0,66	Jun 2017 – Aug 2017	0.34	0.39

455